Available online at www.sciencedirect.com
ScienceDirect
Progress in Natural Science 19 (2009) 759–767
Progress in Natural Science
www.elsevier.com/locate/pnsc

An improved exponential filter for fast nonlinear registration of brain magnetic resonance images

Zhiying Long [a], Li Yao [a,b,*], Kewei Chen [c], Danling Peng [a]

[a] State Key Laboratory of Cognitive Neuroscience and Learning, Beijing Normal University, Beijing 100875, China
[b] School of Information Science and Technology, Beijing Normal University, Beijing 100875, China
[c] Banner Alzheimer Institute (BAI) & Samaritan PET Center, Phoenix, AZ, USA

Received 18 April 2008; received in revised form 10 June 2008; accepted 13 June 2008

Abstract

A linear elastic convolution filter was derived from the eigenfunctions of the Navier–Stokes differential operator by Bro-Nielsen in order to match images with large deformations. Due to the complexity of constructing the elastic convolution filter, the algorithm's efficiency reduces rapidly with the increase in the image's size. In our previous work, a simple two-sided exponential filter with high efficiency was proposed to approximate an elastic filter. However, its poor smoothness may degenerate the performance. In this paper, a new exponential filter was constructed by utilizing a modified nonlinear curve fitting method to approximate the elastic filter. The new filter's good smoothness makes its performance comparable to an elastic filter. Its simple and separable form makes the algorithm's speed faster than the elastic filter. Furthermore, our experiments demonstrated that the new filter was suitable for both the elastic and fluid models.

Keywords: Exponential filter; Nonlinear; Registration; Magnetic resonance imaging

1. Introduction

Image registration in neuroimaging studies, which aims at matching an image onto another with optimal spatial transformation, has a variety of applications. In a medical imaging study, for example, functional or structural changes in images of an individual subject over time need to be examined, or images of a patient group and a normal control group need to be compared. Because of the inter-subject neuroanatomy variation, it is necessary to perform image registration before these statistical comparisons. The registration algorithms can be categorized as linear or nonlinear. The simple linear registration, such as rigid or affine transformation, only removes global differences in brain shape and size. In contrast, nonlinear registration eliminates local differences of the two images. In many cases, both algorithms are used, linear alignment prior to nonlinear registration.

Nonlinear registration usually transforms images in higher-dimensional anatomical mapping in order to match local variability across different anatomies [1,2]. Nonlinear registration approaches can be divided into intensity-based and model-based types [3]. The intensity-driven algorithm matches the regional intensity of each image based on mathematical or statistical criteria [4], whereas the model-driven algorithm needs to build geometric models including functionally important surfaces, curves and point marks [5]. For the intensity-driven algorithm, automated image registration [6] and statistical parametric mapping algorithms [7] can measure anatomical differences efficiently by using global basis functions to approximate deformation fields in lower-dimensional anatomical mappings. The transformation's degree of freedom is generally not

* Corresponding author. Tel.: +86 10 58807727.
E-mail address: yaoli@bnu.edu.cn (L. Yao).

1002-0071/$ - see front matter © 2009 National Natural Science Foundation of China and Chinese Academy of Sciences. Published by Elsevier Limited and Science in China Press. All rights reserved.
doi:10.1016/j.pnsc.2008.06.028

beyond the order of basis functions. Due to lower-dimensional mapping, the limited basis functions fail to approximate the deformation totally. However, in higher-dimensional anatomical mappings, physical continuum models allow extremely flexible deformations, and the degrees of freedom can be as many as the number of voxels in the images.

Various numerical algorithms and mathematical models in the field of physics have been adopted to the nonlinearly register image of one subject to that of another [8–11]. Relevant to our current efforts, a brief review of the two approaches based on the elastic solid model and the viscous fluid model, respectively, is in demand and provided here. Physical continuum models were introduced for use in nonlinear registration because they allow for extremely flexible deformations and their degrees of freedom can be as many as the number of voxels in images [3]. Bajcsy and Kovacic et al. [12], based on the physical continuum model, were the first to construct the deforming image as a 3D elastic solid and to derive the body force from the gradient of the intensity correlation. Continuing their efforts and recognizing the limitation of small deformation assumptions for the linear elastic model, Christensen [13,14] proposed a viscous fluid model to estimate large image deformations for maintaining the continuity of structures. This model overcomes two pitfalls of the elastic model: linear elastic penalties and small deformation approximations. Therefore, the fluid model can perform large-magnitude displacement. However, because the viscous fluid partial differential equation (PDE) has to be solved on a discrete lattice, the speed of the algorithm is too slow to be implemented on the PC [15].

Based on the work of Christensen [13], Bro-Nielsen and Gramkow [15] derived a convolution filter for linear elasticity from the eigenfunctions of the Navier–Stokes differential operator $L = \mu\nabla^2 + (\lambda + \mu)\nabla(\nabla^T)$. This filter increased the algorithm speed in the fluid model by several orders of magnitude. Unfortunately, the computation time for constructing the filter and performing the convolution operation increased exponentially with the size of the image. Therefore, it is desirable to derive alternative computationally efficient filters. In fact, Bro-Nielsen and Gramkow [15] demonstrated that the 'demon'-based registration method [9,16] is actually equivalent to the use of a Gaussian filter as an approximation of the elastic filter. The increased computing efficiency associated with the Gaussian filter is due to the fact that a 2D or 3D Gaussian filter is the product of two or three one-dimensional Gaussian filters, which can be referred to as separatability. Due to the notable differences between the Gaussian and elastic filters, however, one should not expect the same or similar performance with the use of these two filters [15,17].

Balancing the increased efficiency and better performance than the Gaussian filter, we previously proposed a simple two-sided exponential filter and demonstrated, indeed, that its performance is superior to the Gaussian filter and its computational efficiency is higher than both the elastic filter and the Gaussian filter [18]. Nevertheless, there are some limitations to the two-sided exponential filter. For example, its smoothness is poor. Consequently, it may not be as robust as an elastic filter. Continuing our efforts, the current study proposes (i) to use a new curve fitting method to produce a new exponential filter that has much higher computational efficiency than an elastic filter, but has almost the same performance and robustness as an elastic filter; (ii) to generalize its use from vicious fluid model to also elastic model. This generalization is possible as the two models can be unified under the framework of the Navier–Stokes equilibrium equations. Excellent matching results are obtained by using the new exponential filter in both models.

2. The unification of elastic and fluid models

2.1. Image registration based on elastic and fluid models

The general theory will be illustrated for the 2D case, but it is applicable to 3D as well. We assume that the two images, an object image (O) and a template image (T), are to be registered. This registration is via an optimized smooth deformation field $\boldsymbol{u}(\boldsymbol{x}, t)$ mapping the coordinate space of O to that of T.

2.1.1. The elastic model

In elastic media, the 2D displacement field $\boldsymbol{u}(\boldsymbol{x}, t)$ resulting from internal deformation forces $\boldsymbol{F}(\boldsymbol{x}, t)$, which is called body force, obeys the Navier–Stokes equilibrium equation for linear elasticity [1]:

$$\mu\nabla^2\boldsymbol{u}(\boldsymbol{x}, t) + (\lambda + \mu)\nabla(\nabla^T \cdot \boldsymbol{u}(\boldsymbol{x}, t)) + \boldsymbol{F}(\boldsymbol{x}, t) = 0 \quad \forall \boldsymbol{x} \in \boldsymbol{R}^2 \tag{1}$$

where $\nabla^T \cdot \boldsymbol{u}(\boldsymbol{x}, t) = \sum \partial u_j / \partial x_j$, $\nabla^2 = \nabla^T\nabla$ is the Laplacian operation, and Lamé's coefficients, λ and μ, refer to the elastic properties of the medium. Eq. (1) describes the displacement of a particle at location x when time is t assuming that the particle is of extremely small size. Moreover, in the study of medical image registration, body force is derived from the gradient of a cost function, such as intensity correlation.

In order to use this model, the displacement of each particle is assumed to be small. So the model is more suitable for image registration with small deformation on a region-by-region basis (not global position difference).

2.1.2. The fluid model

Christensen [13] introduced the fluid model to describe large distance deformations. Under the external body force $\boldsymbol{F}(\boldsymbol{x}, \boldsymbol{u}(\boldsymbol{x}, t))$, the particles of the fluid move with the instantaneous velocity $\boldsymbol{v}(\boldsymbol{x}, t)$ determined by the deformation field $\boldsymbol{u}(\boldsymbol{x}, t)$. The body force and velocity also satisfy the Navier–Stokes equilibrium equation.

$$\mu\nabla^2\boldsymbol{v}(\boldsymbol{x}, t) + (\lambda + \mu)\nabla(\nabla^T \cdot \boldsymbol{v}(\boldsymbol{x}, t)) + \boldsymbol{F}(\boldsymbol{x}, \boldsymbol{u}(\boldsymbol{x}, t)) = 0 \tag{2}$$

Comparing Eq. (1) with Eq. (2), it is obvious that the two models obey the same Navier–Stokes equilibrium equation noting the major difference between them is that $\boldsymbol{u}(\boldsymbol{x})$ in Eq. (1) is replaced with $\boldsymbol{v}(\boldsymbol{x},t)$ in Eq. (2).

2.2. Convolution filter in the solution of the Navier–Stokes equation

Regardless of the models, PDE must be solved in order to obtain the deformation field. It is a computationally expensive process if the algorithm of Christensen is used. Bro-Nielsen proposed the convolution filter approach to solve the linear PDE [15]. Comparing Eq. (1) with Eq. (2), the common Navier–Stokes differential operator L is

$$L = \mu\nabla^2 + (\lambda+\mu)\nabla(\nabla^T). \tag{3}$$

Under the linear operator L, the elastic and fluid models are expressed as

$$L\boldsymbol{u}(\boldsymbol{x},t) + \boldsymbol{F}(\boldsymbol{x},t) = 0 \quad L\boldsymbol{v}(\boldsymbol{x},t) + \boldsymbol{F}(x,\boldsymbol{u}(\boldsymbol{x},t)) = 0 \tag{4}$$

Eq. (4) suggests that the two models can be described using a uniform system with an external body force as the input $\boldsymbol{F}$. The output is $\boldsymbol{u}(\boldsymbol{x})$ for the elastic model and $\boldsymbol{v}(\boldsymbol{x},t)$ for the fluid model, respectively (Fig. 1(a)).

As shown in Fig. 1(a), with the availability of the convolution filter, $\boldsymbol{H}$, the solution of Eq. (1) or Eq. (3) is simply $\boldsymbol{F}$ convolved with $\boldsymbol{H}$. Based on the eigenfunctions of the linear operator L, Bro-Nielsen derived the filter $\boldsymbol{H}$ as an approximation to the impulse response of an applied unit force in the middle of the square with a unit area (defined as $[0\,1]\times[0\,1]$). To make it applicable to images with a finite number of voxels, the filter is discretized. Assume that the image size is $D \times D$, and let the lattice be addressed by $\boldsymbol{x}=[x_1,x_2]^{\mathrm{T}}$, where $\boldsymbol{x}_r \in [-\frac{D-1}{2},\frac{D-1}{2}],\ r=1,2$.

The filter implementing the 2D linear elastic operator L for the unit force in the x_1 direction applied in $\boldsymbol{x}_c$ is then [15]

$$\boldsymbol{H}_1(\boldsymbol{x}) = \frac{4}{\pi^2\mu(2\mu+\lambda)}\sum_{i,j=0}^{D-1}\frac{p(\boldsymbol{x}_c)}{(i^2+j^2)^2\Gamma_{ij}}\begin{bmatrix}-(i^2\mu+(2\mu+\lambda)j^2)p(\boldsymbol{x})\\(\mu+\lambda)ijq(x)\end{bmatrix} \tag{5}$$

$$p(\boldsymbol{x}) = \sin(i\pi x_1)\cos(j\pi x_2) \quad q(\boldsymbol{x}) = \cos(i\pi x_1)\sin(j\pi x_2) \tag{6}$$

$$\Gamma_{ij} = \begin{cases}1 & \text{if none of } i,j \text{ are zeros}\\ 2 & \text{for one of } i,j \text{ is zeros}\end{cases} \tag{7}$$

Apparently, the computational cost increases dramatically as a function of the image size. The linear elastic filter for the 3D case is very complex. And the detailed derivation of the 3D filter can be referred to [19].

Note that, $\boldsymbol{H}_2(\boldsymbol{x})$, the filter with unit force applied to the x_2 direction can be obtained from $\boldsymbol{H}_1(\boldsymbol{x})$ by switching x_1 and x_2 positions. Then the filter with a unit force of (f_x,f_y) is obtained as $f_x \otimes \boldsymbol{H}_1(\boldsymbol{x}) + f_y \otimes \boldsymbol{H}_2(\boldsymbol{x})$, where $\otimes$ is the convolution operation.

2.3. Properties of the linear elastic filter

With the linearity and symmetry of $\boldsymbol{H}_1$ and $\boldsymbol{H}_2$, we only need to discuss $\boldsymbol{H}_1$ here. Appropriate values of viscosity coefficients λ and μ depend upon the particular imaging modality. Here we take $\lambda = 11.5$ and $\mu = 1$. As $\boldsymbol{H}_1(\boldsymbol{x})$ is a vector field, it has one component, $H_1^{x_1}(\boldsymbol{x})$ along the x_1 direction and another component $H_1^{x_2}(\boldsymbol{x})$ along the x_2 direction (Fig. 1(b)). Because $\boldsymbol{H}_1(\boldsymbol{x})$ is associated with a unit force acting in the x_1 direction, $H_1^{x_1}(\boldsymbol{x})$ has a much larger magnitude than $H_1^{x_2}(\boldsymbol{x})$ that is often ignored for simplicity. A scalar field $H_1^{x_1}(\boldsymbol{x})$ symmetrical along the x_1 and x_2 directions is depicted in Fig. 1(c).

Because a unit force acts in the center of the image, the displacement of the center is much larger than that of the peripheral areas. For the image size 128×128, the middle column curve $H_1^{x_1}(0.5,\boldsymbol{x}_2)$ with $x_1 = 0.5$ can be extracted from $H_1^{x_1}(\boldsymbol{x})$. The same is for the middle row curve $H_1^{x_1}(\boldsymbol{x}_1,0.5)$ when $x_2 = 0.5$. These two curves almost dominate the whole scalar field (Fig. 2(a)). Curves of similar shapes, but with reduced magnitudes, are observed moving toward the edges of images from its center.

3. New exponential filter

3.1. Curve fitting method

Obviously, it is computationally expensive to construct a linear elastic filter based on Eq. (9), especially for the images with a high number of voxels. Motivated by the exponential-like shapes of the curves as shown in Fig. 2(a) simpler exponential filters could be utilized to approximate the complex elastic filter with an additional assumption that the convolution filter can be expressed as

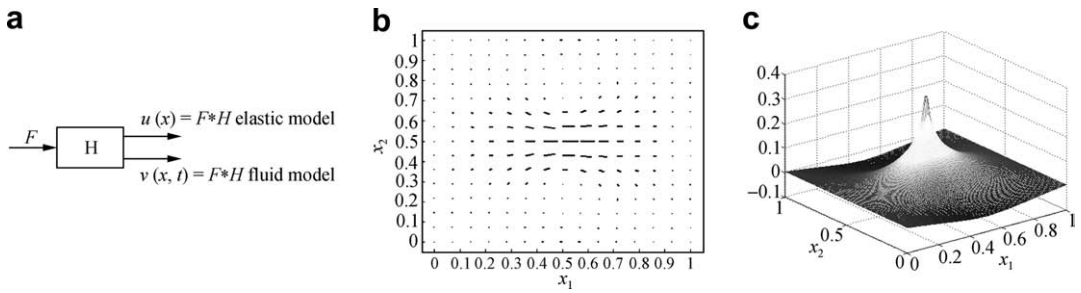

Fig. 1. (a) The uniform system model. $\boldsymbol{H}$ is the system function referred to as the linear convolution filter; (b) displacement vector field $H_1(\boldsymbol{x})$ with size 15×15; (c) the scalar field $H_1^{x_1}(\boldsymbol{x})$ of $H_1(\boldsymbol{x})$ shown in 3D space with size 128×128.

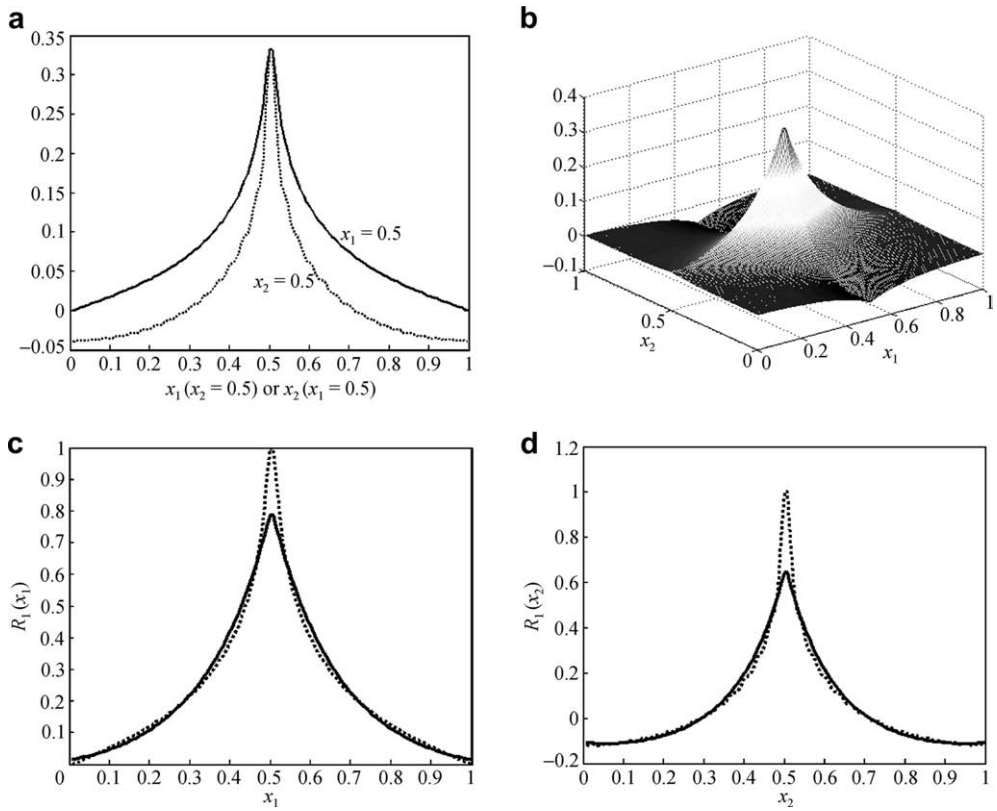

Fig. 2. (a) Two curves of $H_1^{x_1}(0.5, \boldsymbol{x}_2)$ (solid line) and $H_1^{x_1}(\boldsymbol{x}_1, 0.5)$ (dotted line); (b) a new 2D exponential filter $H_1^{x_1}(x_1, x_2)$ in a 3D space; (c) the original curve (dotted line) and the fitted curve (solid lines) of the normalized curve of $H_1^{x_1}(0.5, \boldsymbol{x}_2)$; (d) the original curve (dotted line) and the fitted curve (solid lines) of the normalized curve of $H_1^{x_1}(\boldsymbol{x}_1, 0.5)$.

a production of a function of x_1 and a function of x_2 (i.e., the filter is x_1–x_2 separable).

Let $R_1(x_1)$ represent the row curve with D data points (x_{i1}, x_{i2}), we wish to find a function of x_1 and parameter p that gives the "best fit" to the data by the function $F(x_1,p)$. Here $F(x_1,p)$ is assumed to have an exponential form.

$$F(x_1,p) = \mathrm{e}^{g(x_1,p)} \quad g(x_1,p) = p_1 x_1^2 + p_2|x_1| + p_3 \tag{8}$$

The exponent $g(x_1,p)$ is a quadratic polynomial. The data-fitting can be transformed into the linear relation by taking the logarithm on both sides of Eq. (8).

$$\ln F(x_1,p) = g(x_1,p) \tag{9}$$

In order to assure that $F(x_1,p)$ is larger than zero, $R_1(x_1)$ is first normalized by making the maximum equal to 1 and then a constant is added to it.

$$R_1'(x_1) = \frac{R_1(x_1)}{\max(R_1(x_1))} + C \quad R_1'(x_1) > 0 \tag{10}$$

The nonlinear data-fitting method is to find the function $g(x_1,p)$ that best fits the transformed data points $\ln R_1'(x_1)$ in the least squares sense.

$$\min_{x_1} \sum_{i=1}^{D} (\ln R_1'(x_{1i}) - g(x_{1i},p)) \tag{11}$$

If we define a matrix $\boldsymbol{A}$ with $A = [x_1^2 \mid x_1 \mid 1]$ and vector $\boldsymbol{b}$ with components $b_i = \ln R_1'(x_{1i})$, then the data-fitting problem takes the form

$$Ap \cong b \tag{12}$$

The least squares estimate of Eq. (12) is $\tilde{p} = (\boldsymbol{A}^T\boldsymbol{A})^{-1}\boldsymbol{A}^T\boldsymbol{b}$. The normalized data can be expressed as

$$\tilde{R}_1'(x_1) = R_1'(x_1) - C = e^{g(x_1\tilde{p})} - C = e^{\tilde{p}_1 x_1^2 + \tilde{p}_2 x_1 + \tilde{p}_3} - C \tag{13}$$

Using the same method described above, the column curve can also be fitted.

$$\begin{aligned}\tilde{R}_1'(x_2) &= R_1'(x_2) - C' = e^{g(x_2,\tilde{p}')} - C' \\ &= e^{\tilde{p}_4 x_2^2 + \tilde{p}_5 x_2 + \tilde{p}_6} - C'\end{aligned} \tag{14}$$

The new 2D filter for the x_1 direction can be derived by combining Eq. (13) with Eq. (14).

$$H_1^{x_1}(x_1,x_2) \cong k\tilde{R}_1'(x_1)\tilde{R}_1'(x_2) \quad 0 < k \leqslant 1 \tag{15}$$

$$k = \frac{\max(H_1^{x_1}(x_1,x_2))}{\max(\tilde{R}_1'(x_1))\max(\tilde{R}_1'(x_2))} \tag{16}$$

The impulse response for the x_2 direction is determined by the simple rotation of that for the x_1 direction.

$$H_2^{x_2}(x_1,x_2) \cong k\tilde{R}_2'(x_1)\tilde{R}_2'(x_2) \quad 0 < k \leqslant 1 \tag{17}$$

$$\tilde{R}_2'(x_1) = e^{\tilde{p}_4 x_1^2 + \tilde{p}_5 x_1 + \tilde{p}_6} - C' \tag{18}$$

$$\tilde{R}_2'(x_2) = e^{\tilde{p}_1 x_2^2 + \tilde{p}_2 x_2 + \tilde{p}_3} - C \tag{19}$$

Here, the subscripts 1 and 2 of $H(x_1,x_2)$ denote that the center unit force comes from the x_1 and x_2 directions, respectively. k is an amplitude coefficient.

3.2. The coefficients of a new exponential filter

Applying the method in Section 3.1 to the elastic filter with 128×128 size, the new filter's coefficients can be derived. For $R_1'(x_1)$, the x_1 coordinate is set to between 0 and 1. The coefficients are $\tilde{p} = [0.0003\ -0.0404\ 0.0092]$. For $R_2'(x_2)$, the coefficients are $\tilde{p}' = [0.0005\ -0.0575\ -0.0290]$. Fig. 2(c) and (d) shows the fitted curves.

The new 2D exponential filter $H_1^{x_1}(x_1,x_2)$ is derived simply from Eq. (15), and is shown in Fig. 2(b). Here $k = 0.6538$.

3.3. Variation of the parameters with the image size

To see how image size affects the values of the estimated parameters, we plotted each of the six estimated parameter values vs. the number of voxels varying from 32 to 200 with an increment of 4 (see Fig. 3). Furthermore, we investigated their relationship by constructing each of the six parameters as a function of the image size using the least square fit. The expressions of all functions are in the following. Here p_1, p_2 and p_3 are the parameters of Eq. (13), while p_4, p_5 and p_6 correspond to those of Eq. (14).

$$p_1(x_1) = \frac{1}{0.2145x_1^2 + 1.3856x_1 + 252.5768}$$

$$p_2(x_1) = \frac{-1}{0.1912x_1 + 0.4223} \tag{20}$$

$$p_3(x_1) = \frac{-\lg(0.008x_1 - 0.084)}{3}$$

$$p_4(x_2) = \frac{1}{0.1378x_2^2 - 2.7417x_2 + 73.0772} \tag{21}$$

$$p_5(x_2) = \frac{1}{-0.1542x_2 + 2.1662}$$

$$p_6(x_2) = \frac{-\lg(0.0126x_2 - 0.3871)}{3} \tag{22}$$

Fig. 3 suggests that all functions of Eqs. (20)–(22) describe the variation of parameters with image size very well. To further validate the use of these fitted functions, we compared the calculated parameter values based on these functions and those directly estimated from the image size of 256×256. The six parameters calculated from the above functions were $p_1 = 6.8191\text{e-}005$, $p_2 = -0.0203$, $p_3 = -0.0977$, $p_4 = 1.1902\text{e-}004$, $p_5 = -0.0268$ and $p_6 = -0.1510$. The parameters estimated directly were $p_1 = 0.0001$, $p_2 = -0.0199$, $p_3 = -0.1000$, $p_4 = 0.0001$, $p_5 = -0.0260$ and $p_6 = -0.1501$. We found that they were comparable.

3.4. Algorithms of elastic and fluid registration based on the new filter

The complete elastic registration algorithm procedure consists of the following steps:

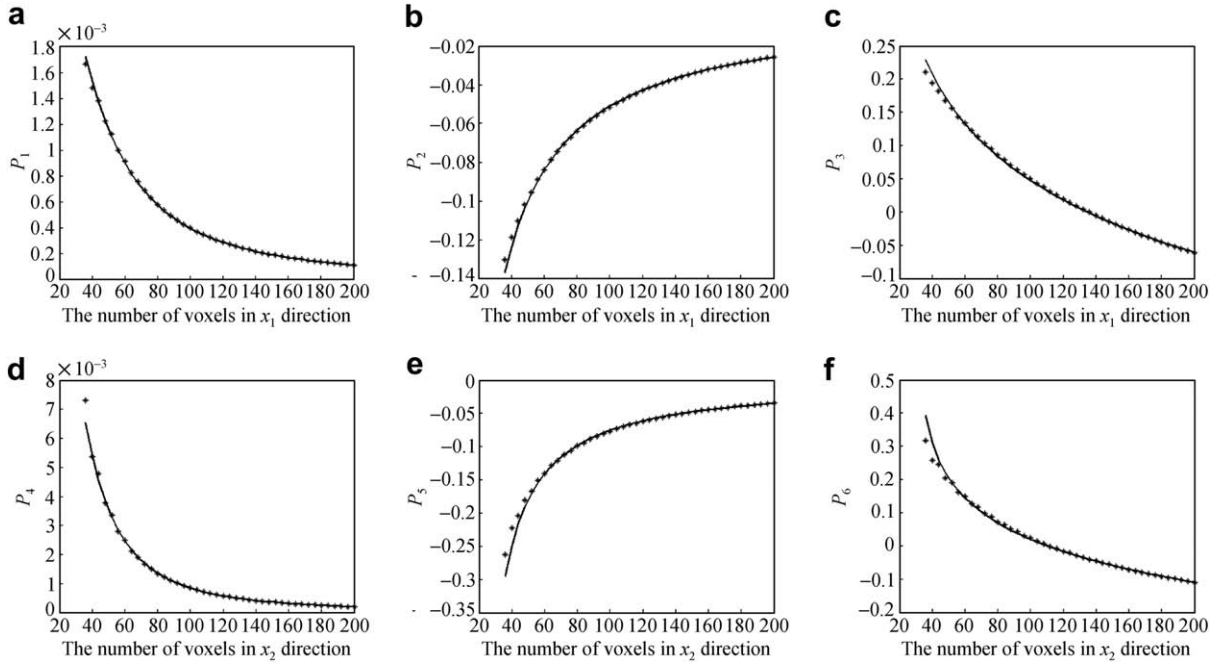

Fig. 3. Plots of parameters vs. the number of voxels in each direction. The * markers represent original data points, and the solid lines are the curves of fitted functions.

(1) Produce a new filter $\boldsymbol{H}(\boldsymbol{x})$ including $H_1^{x_1}(x_1,x_2)$ and $H_2^{x_2}(x_1,x_2)$ using Eq. (15) and Eq. (17);
(2) Let $t = 0$ and $\boldsymbol{u}(\boldsymbol{x},\boldsymbol{t}) = 0$;
(3) Calculate the body force $\boldsymbol{F}(\boldsymbol{x}, \boldsymbol{u}(\boldsymbol{x},t))$ using Eq. (5);
(4) If $\boldsymbol{F}(\boldsymbol{x}, \boldsymbol{u}(\boldsymbol{x},t))$ is below a threshold for all $\boldsymbol{x}$, then stop;
(5) Convolve filter $\boldsymbol{H}(\boldsymbol{x})$ with $\boldsymbol{F}(\boldsymbol{x}, \boldsymbol{u}(\boldsymbol{x},t))$ to obtain the displacement field $\boldsymbol{u}(\boldsymbol{x},t)$;
(6) $t = t + 1$, go to 3.

The fluid registration algorithm is more complex than the elastic registration because we must apply Euler integration over time using a forward finite difference estimate of the time derivative in Eq. (4) in order to calculate the displacement $\boldsymbol{u}(\boldsymbol{x},t)$:

$$\boldsymbol{u}(\boldsymbol{x},t+\Delta) = \boldsymbol{u}(\boldsymbol{x},t) + \Delta \boldsymbol{v}(\boldsymbol{x},t)\sum_{i=1}^{3} v_i(\boldsymbol{x},t)^{\partial \boldsymbol{u}(\boldsymbol{x},t)}/\partial x_i \qquad (23)$$

(1) Produce the $\boldsymbol{H}(\boldsymbol{x})$ including $H_1^{x_1}(x_1,x_2)$ and $H_2^{x_2}(x_1,x_2)$ using Eq. (15) and Eq. (17);
(2) let $i = 0$ and $\boldsymbol{u}(\boldsymbol{x},0) = 0$;
(3) calculate the body force $\boldsymbol{F}(\boldsymbol{x}, \boldsymbol{u}(\boldsymbol{x},t_i))$ using Eq. (5);
(4) if $\boldsymbol{F}(\boldsymbol{x}, \boldsymbol{u}(\boldsymbol{x},t_i))$ is below a threshold for all $\boldsymbol{x}$, then stop;
(5) convolve filter $\boldsymbol{H}(\boldsymbol{x})$ with $\boldsymbol{F}(\boldsymbol{x}, \boldsymbol{u}(\boldsymbol{x},t_i))$ to get the instantaneous velocity $\boldsymbol{v}(\boldsymbol{x},t_i)$;
(6) calculate the perturbation of the displacement field.

$$\boldsymbol{R}(x) = \boldsymbol{v}(\boldsymbol{x},t_i) - \sum_{i=1}^{3} v_i(\boldsymbol{x},t_i)^{\partial \boldsymbol{u}(\boldsymbol{x},t_i)}/\partial x_i \qquad (24)$$

(7) choose a time step Δ $\max(\|\boldsymbol{R}(\boldsymbol{x})\|) < du_{\max}$, where $du_{\max}$ is the maximal flow allowed in one iteration and $\Delta = t_{i+1} - t_i$;
(8) if the Jacobian $J = |x - u(x,\ t_{i+1})| < 0.5$, then regrid the object image and let $\boldsymbol{u}(\boldsymbol{x},\ t_{i+1}) = 0$. Otherwise calculate $\boldsymbol{u}(\boldsymbol{x},\ t_{i+1})$ using Eq. (23);
(9) let $i = i + 1$ and go to 3.

4. Experiment

Simulated imaging data and real MRI data were used to demonstrate how the new filter accommodates both the elastic and fluid models and how its performance fared against the elastic filter. Two sets of simulated data using the binary image with a size of 128×128 were used in 2D elastic and fluid registration [13,15]. Real MRI data were used to compare the performance between elastic and fluid registration through two sorts of filters.

Among these data, it was assumed that the object and the template images were consistent on topology and that each constituent structure had roughly the same gray-level values.

4.1. 2D elastic image registration

The object image is a square and the template is a rectangle. The dimension of these images is 128×128 pixels. The square is 34×34 and the rectangle is 34×58. In [15], an elastic filter was used to match the square with the rectangle based on the fluid model. Because the difference between the two images was not large, the elastic model is also suitable for matching these two images. Both the new filter and the elastic filter were applied to transform the square. Results in Fig. 4(a) show that the performance of the new filter is almost the same as the elastic filter, and the new filter can maintain the topology of the deformed image as well as the elastic filter. For the sake of the convergence speed comparison, the mean square error between the template image and the deformed object image was calculated at each iteration. Fig. 4(b) shows that the iterative convergence speed of the new filter is a little bit faster than the elastic filter during the first 50 iterations.

4.2. 2D fluid image registration

The simulated data used here are similar to that of Christensen [13]. The template is a "C"-shaped image with 128×128 pixels, and the object is a wedge-shaped image. The two images were first linearly aligned so that they overlapped. Then both the elastic and fluid models were used to register the images. The result shows that the elastic model is no longer suitable in the large deformation. On the other hand, the new filter performed equally well on the vicious fluid model (Fig. 5(a)). The convergence speed of the two filters based on the fluid model is almost the same (Fig. 5(b)).

4.3. 2D MRI data registration

We applied elastic and fluid models to real 2D MRI data of the human brain by using both the new and the elastic filters. Both object and template images were from one slice of each two 3D MRI data. The 3D template image was a single-subject T1 template in SPM software (http://www.fil.ion.ucl.ac.uk/spm/) with $91 \times 109 \times 91$ voxels at $2 \times 2 \times 2\ \mathrm{mm}^3$. The 3D object was a T1 image of a single subject with $77 \times 220 \times 220$ voxels at $2 \times 1 \times 1\ \mathrm{mm}^3$. First, the 3D object image was resampled into the dimension of the template and aligned with the template in a global shape by a simple linear affine transformation. The axial slices 48 of both T1 images in transverse view were selected. The range of intensity in the 2D object image was preprocessed by histogram-matching it to the template image. The final results are shown in Fig. 6(a).

Great differences can be found in the ventricles of the object and template image. A mask of ventricle is constructed to compare the differences in ventricle area between template and deformed image. For the elastic model, the mean square error of the ventricle area was 0.0162 with the new filter and 0.0248 with the elastic filter.

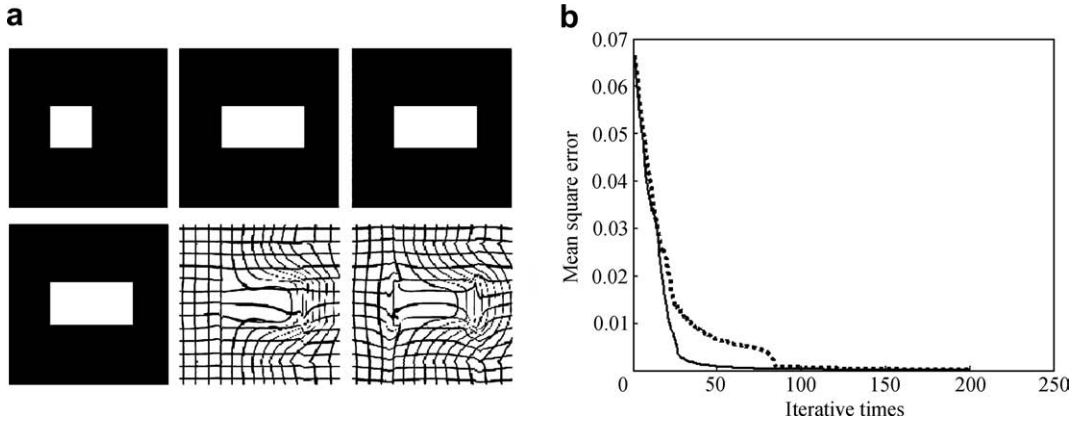

Fig. 4. Results of the 2D elastic image registration. (a) The left column corresponds to the object (top) and template images (bottom). The middle column shows the deformed object images (top) and rectangular grids (bottom) after the elastic transformation with the new filter. The right column shows the deformed object images (top) and rectangular grids (bottom) with the elastic filter. (b) Mean squared error vs. iterative times (before 100 times). The solid line represents the convergence curve of the new filter, and the dotted line represents that of the elastic filter.

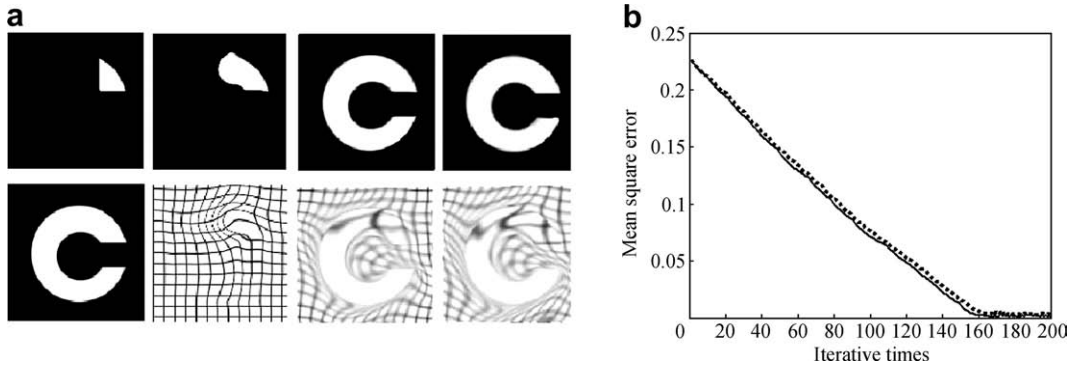

Fig. 5. Results of the 2D fluid image registration. (a) The leftmost column shows the object (top) and template image (bottom). The left center column shows the deformed object image (top) and a rectangular grid (bottom) after the elastic transformation with the new filter. The right center column shows the deformed object image (top) and a rectangular grid (bottom) after a fluid transformation with the new filter. The rightmost column shows the deformed object image (top) and a rectangular grid (bottom) after a fluid transformation with the elastic filter. (b) Mean squared error vs. iterative times based on the fluid model. The solid line represents the convergence curve of the new filter, and the dotted line represents that of the elastic filter.

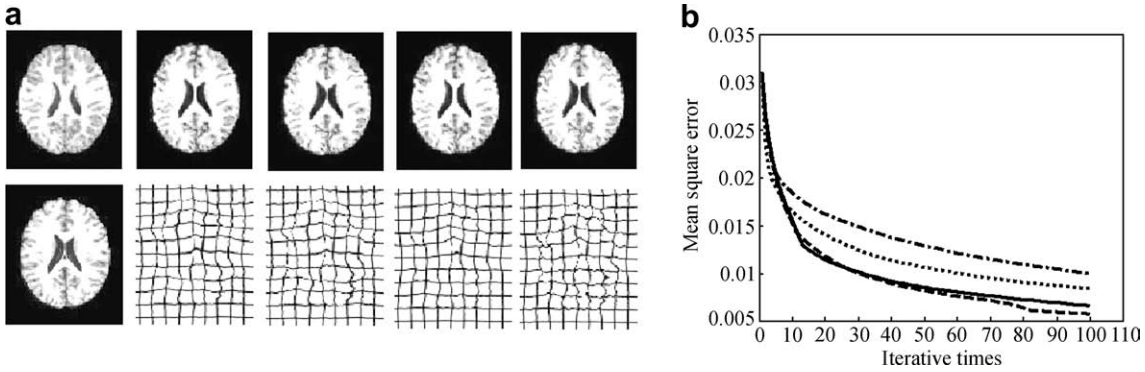

Fig. 6. Results of the 2D MRI data registration. (a) The first column shows the object (top) and template image (bottom). The second column shows the deformed object images (top) and a rectangular grid (bottom) after the elastic transformation with the new filter. The third column shows the deformed object images (top) and a rectangular grid (bottom) after the fluid transformation with the new filter. The fourth column shows the deformed object images (top) and a rectangular grid (bottom) after the elastic transformation with the elastic filter. The fifth column shows the deformed object images (top) and a rectangular grid (bottom) after the fluid transformation with the elastic filter. (b) Mean squared error vs. iterative times (before 100 times). The solid line represents the convergence curve of the fluid transformation with the new filter, the dashed line represents that of the fluid transformation with the elastic filter, the dotted line represents that of the elastic transformation with the new filter and the dash dotted line represents that of elastic transformation with the elastic filter.

Table 1
Mean and SD for the two filters.

Filter	Total time (s)	Iterative steps
Elastic filter	87 ± 17.4	304 ± 64
New filter	38 ± 9.6	133 ± 35

For the fluid model, it was 0.0131 with the new filter and 0.0133 with the elastic filter. Thus, the results of the fluid model with two filters are better than those of the elastic model. Fig. 6(b) shows that the convergence speed of the new filter is close to that of the elastic filter based on the fluid model, while it is faster for the new filter than the elastic filter based on the elastic model.

In order to evaluate the algorithm efficiency of the two filters on elastic model further, 18 subjects' 2D MRI data were selected with the same method. No significant difference existed in the initial mean square errors between each subject's 2D image and template. All these 2D MRI data were registered to the same template image. The terminative threshold of mean squared error was set to 0.005. The total time for the whole iterations was recorded for each subject. As the same fast convolution algorithm provided by Matlab was used, the two filters would take almost the same time in each iterative step. Consequently, both the total time and steps taken in the whole iterations can be used to indicate the speed of convergence. Table 1 lists the mean and standard deviation (SD) of time and step for the two filters. Results in Table 1 provide an additional support for the faster convergence speed of the new filter than the elastic filter in the elastic model.

5. Discussion

5.1. Separation of the new exponential filter

One main advantage of the new filter is that it is separable along any direction. The property makes the convolution operation much easier and reduces the time cost greatly in images with a large size. In general discrete 2D convolution $F = H * G$,

$$F(x_1, x_2) = \sum_m \sum_n H(m,n) G(x_1 - m, x_2 - n) \tag{25}$$

If $H(m,n)$ is separable in x_1 and x_2 directions, it can be expressed as

$$H(m,n) = H(m) * H(n) \tag{26}$$

Now replacing $H(m,n)$ in Eq. (25) with Eq. (26), Eq. (25) becomes

$$\begin{aligned} F(x_1, x_2) &= \sum_m \sum_n H(m)H(n) G(x_1 - m, x_2 - n) \\ &= \sum_m H(m) \sum_n H(n) G(x_1 - m, x_2 - n) \end{aligned} \tag{27}$$

$$U(x_1 - m) = \sum_n H(n) G(x_1 - m, x_2 - n) \tag{28}$$

Eq. (28) is equal to a one-dimensional convolution in the x_2 direction. The initial 2D convolution now becomes

$$F(x_1, x_2) = \sum_m H(m) U(x_1 - m) \tag{29}$$

Therefore, if $H(m,n)$ is separable in two directions, the traditional 2D convolution can be converted into 1D convolution along x_1 and x_2 directions in turn. It is obvious that such separability can simplify the convolution operation and reduce the computation greatly.

5.2. Comparison of the new exponential filter with the two-sided exponential filter

In our previous work [18], we proposed a simple two-sided exponential filter Eq. (30) to register images with high efficiency.

$$H_1(x_1, x_2) = k e^{-\alpha_1 |x_1|} e^{-\alpha_2 |x_2|} \qquad 0 < k \leqslant 1 \tag{30}$$

The new filter is expressed as

$$H_1(x_1, x_2) = k e^{p_1 x_1^2 + p_2 |x_1| + p_3} e^{p_4 x_2^2 + p_5 |x_2| + p_6} \qquad 0 < k \leqslant 1 \tag{31}$$

Because the new filter in Eq. (31) contains both the first-order and second-order exponentials, its smoothness is much better and closer to the elastic filter than the first-order exponential filter such as the two-sided exponential in Eq. (30). It is evident that smooth transformation is essential in the nonlinear registration for the sake of maintaining the continuity of the mapping and preserving the topology of images. That is the smoother the filter, the more robust the transform can be. Therefore, the two-sided exponential filter may not preserve the topology of the images in some complicated cases during nonlinear deformation due to its poor smoothness.

5.3. Selection of viscosity coefficients λ and μ

In our work, λ and μ were set fixed, that is $\lambda = 11.5$ and $\mu = 1$. From the above experiments, we find that the values are fit for both the binary images and real MRI images' registration. Nevertheless, for some other image modalities, these two values for viscosity coefficients may not be suitable any more. Here a simple description is given to illustrate how the parameters of the new exponential filter are affected by only altering μ for simplicity. It is assumed that the image size is 128×128. Table 2 shows how the parameters of the new filter vary with μ. In contrast to p_3, p_6, and k, p_1, p_2, p_4 and p_5 change very slightly with μ. In fact, p_3, p_6 and k mainly control the magnitude of the filter. The difference among them is that k determines the filter's global magnitude, while p_3 and p_6 determine the local magnitude along the x_1 and x_2 directions. Compared with k, the variation of p_3 and p_6 is much smaller than that of k. Therefore, p_3 and p_6 will not have much influence on the filter's shape. Parameter k would actually control the global magnitude of the displacement field instead of the field's

Table 2
Variation of parameters with μ.

μ and λ	p_1	p_2	p_3	p_4	p_5	p_6	k
$\mu = 1$; $\lambda = 11.5$	−0.0003	0.0404	−0.0092	−0.0005	0.0575	0.0290	0.4989
$\mu = 3$; $\lambda = 11.5$	−0.0002	0.0383	0.0029	−0.0005	0.0499	0.0134	0.1878
$\mu = 5$; $\lambda = 11.5$	−0.0002	0.0373	0.0090	−0.0004	0.0465	0.0033	0.1205
$\mu = 7$; $\lambda = 11.5$	−0.0002	0.0366	0.0127	−0.0004	0.0446	−0.0032	0.0899

local distribution after the convolution of the filter with a force field. That means that the large k can result in the fast movement of each pixel. As a result, more iterations would be needed under the small k. However, k cannot be increased without any limitation. When the displacement was beyond what the forces can reach, the large deformation would destroy the topology structure and produce worse results. Thus, it should be cautious to select k for other sorts of image modalities. By far, no good way is available to seek an optimal k, just like the viscosity coefficients' selection. Further work should be done to explore how k varies with λ and μ in the future.

6. Conclusion

In this paper, a modified nonlinear curve fitting method was used to approximate the elastic convolution filter, and a new separable convolution filter with good smoothness was produced. Two advantages in the new filter contribute to its better computation efficiency than the elastic filter. First, the construction of the new filter is much easier than the elastic filter because its complication is not varied with the increase in the image size, which can save much time to construct the filter, especially for the image with a large size. Second, the separability of the new filter causes the traditional convolution separable and reduces the time cost in each iterative step. Moreover, our experiment of real MRI data substantiated that the new filter has faster convergence than the elastic filter based on the elastic model even if the same convolution algorithm was used.

It should also be noted that the current new filter does not match the elastic filter precisely. Thus, more work is worthy of being done to improve the property of the new filter further. And the selection parameter k is also an issue that needs to be investigated in more detail later.

Acknowledgements

This work was supported by the National Natural Science Foundation of China (Grant Nos. 60472016 and 60628101) and the National Natural Science Foundation of Beijing (4061004).

References

[1] Ashburner J, Neelin P, Collins DL, et al. Incorporating prior knowledge into image registration. Neuroimage 1977;6:344–52.
[2] Thompson PM, Toga AW. Visualization and animation of abnormal anatomic structure with a deformable probabilistic brain atlas based on random vector field transformations. Med Image Anal 1997;1:271–94.
[3] Thompson PM, Toga AW. A framework for computational anatomy. Comput Visual Sci 2002;5:13–34.
[4] Woods RP, Grafton ST, Watson JDG, et al. Automated image registration. II. Intersubject validation of linear and nonlinear models. J Comput Assist Tomogr 1998;22:155–65.
[5] Amit Y. Graphical shape templates for automatic anatomy detection with applications to MRI brain scans. IEEE Trans Med Imag 1997;16(1):28–40.
[6] Woods RP, Mazziotta JC, Cherry SF. MRI-PET registration with automated algorithm. J Comput Assist Tomogr 1993;17:536–46.
[7] Ashburner J, Friston KJ. Nonlinear spatial normalization using basis functions. Hum Brain Mapp 1999;7:254–66.
[8] Christensen GE, Miller MI, Vannier M. A 3D deformable magnetic resonance textbook based on elasticity. In: AAAI spring symposium series: applications of computer vision in medical image processing. Stanford University; 1994. p. 153–6.
[9] Cachier P, Pennec X, Ayache N. Fast non-rigid matching by gradient descent: study and improvements of the "demons" algorithm. INRIA Technical Report RR-3707; June 1999.
[10] Miller MI, Christensen GE, Amit Y, et al. Mathematical textbook of deformable neuroanatomies. Proc Natl Acad Sci USA 1993;90:11944–8.
[11] Thirion JP. Fast non-rigid matching of medical images. INRIA Internal Report 2547, Project Epidaure, INRIA, France; 1995.
[12] Bajcsy R, Kovacic S. Multiresolution elastic matching. Comput Vision Graph Image Process 1989;46:1–21.
[13] Christensen GE, Rabbitt RD, Miller MI. Deformable templates using large deformation kinematics. IEEE Trans Image Process 1996;5:1435–47.
[14] Christensen GE. Deformable shape models for anatomy. PhD Thesis, Washington University; 1994.
[15] Bro-Nielsen M, Gramkow C. Fast fluid registration of medical images. Lecture notes in computer science, vol. 1131. New York: Springer; 1996. p. 267–76.
[16] Nielsen M, Florack L, Deriche R. Regularization and scale space. INRIA Tech Rep RR-2352; Sep. 1994.
[17] Gramkow C, Bro-Nielsen M. Comparison of three filters in the solution of the Navier-Stokes equation in registration. In: Proc Scandinavian conference on image analysis (SCIA'97); 1997. p. 795–802.
[18] Long Z, Yao L, Peng D. Fast non-linear elastic registration of 2D medical image. LNCS 2004;3216:647–54.
[19] Bro-Nielsen M. Medical image registration and surgery simulation 1997; PhD Thesis; 1997.